



NOTICE

The quality of this microform is heavily dependent upon the quality of the original thesis submitted for microfilming. Every effort has been made to ensure the highest quality of reproduction possible.

If pages are missing, contact the university which granted the degree.

Some pages may have indistinct print especially if the original pages were typed with a poor typewriter ribbon or if the university sent us an inferior photocopy.

Previously copyrighted materials (journal articles, published tests, etc.) are not filmed.

Reproduction in full or in part of this microform is governed by the Canadian Copyright Act, R.S.C. 1970, c. C-30.

AVIS

La qualité de cette microforme dépend grandement de la qualité de la thèse soumise au microfilmage. Nous avons tout fait pour assurer une qualité supérieure de reproduction.

S'il manque des pages, veuillez communiquer avec l'université qui a conféré le grade.

La qualité d'impression de certaines pages peut laisser à désirer, surtout si les pages originales ont été dactylographiées à l'aide d'un ruban usé ou si l'université nous a fait parvenir une photocopie de qualité inférieure.

Les documents qui font déjà l'objet d'un droit d'auteur (articles de revue, tests publiés, etc.) ne sont pas microfilmés.

La reproduction, même partielle, de cette microforme est soumise à la Loi canadienne sur le droit d'auteur, SRC 1970, c. C-30.

THE DETERMINATION OF THE
SUPERCONDUCTING ENERGY GAP
OF GRANULAR LEAD FILMS

by

Peter Mark Geiger

B.S., Xavier University, 1984

A THESIS SUBMITTED IN PARTIAL FULFILLMENT OF
THE REQUIREMENTS FOR THE DEGREE OF
MASTER OF SCIENCE
in the Department
of
Physics

© Peter Mark Geiger 1987

SIMON FRASER UNIVERSITY

November 1987

All rights reserved. This thesis may not be
reproduced in whole or in part, by photocopy
or other means, without the permission of the author

Permission has been granted to the National Library of Canada to microfilm this thesis and to lend or sell copies of the film.

The author (copyright owner) has reserved other publication rights, and neither the thesis nor extensive extracts from it may be printed or otherwise reproduced without his/her written permission.

L'autorisation a été accordée à la Bibliothèque nationale du Canada de microfilmer cette thèse et de prêter ou de vendre des exemplaires du film.

L'auteur (titulaire du droit d'auteur) se réserve les autres droits de publication; ni la thèse ni de longs extraits de celle-ci ne doivent être imprimés ou autrement reproduits sans son autorisation écrite.

ISBN 0-315-42673-X

APPROVAL

Name: Peter M. Geiger

Degree: Master of Science

Title of Thesis: The Determination of the Superconducting
Energy Gap of Granular Lead Films.

Examining Committee:

Chairman: J. C. Irwin

Bruce P. Clayman
Senior Supervisor

Suso Gygax

George Kirczenow

Robert F. Frindt
External Examiner
Professor
Department of Physics
Simon Fraser University

Date Approved: November 27, 1987

PARTIAL COPYRIGHT LICENSE

I hereby grant to Simon Fraser University the right to lend my thesis, project or extended essay (the title of which is shown below) to users of the Simon Fraser University Library, and to make partial or single copies only for such users or in response to a request from the library of any other university, or other educational institution, on its own behalf or for one of its users. I further agree that permission for multiple copying of this work for scholarly purposes may be granted by me or the Dean of Graduate Studies. It is understood that copying or publication of this work for financial gain shall not be allowed without my written permission.

Title of Thesis/Project/Extended Essay

The Determination of the Superconducting

Energy Gap of Granular Lead Films

Author,

(signature)

Peter Mark GEIGER

(name)

December 10, 1987

(date)

ABSTRACT

Measurements have been performed on thermally evaporated lead thin films in order to determine the superconducting energy gap and the critical temperature.

The energy gap measurements were performed using Fourier Transform spectroscopy over the energy region from 5 to 100 cm^{-1} . Transmission measurements were made while the film was in the superconducting and normal states. The ratio of the superconducting state transmission to the normal state transmission was obtained for various sample thicknesses. The critical temperature was determined by measuring the resistivity and magnetization as functions of temperature.

The film was modelled as composed of small grains with different gap energies. The experimentally observed transmission spectra were modelled as due to a combination of transmission through the grains and transmission through gaps between grains, with the gaps between the grains acting as wave guides. The theoretical model incorporates the skin effect for normal and superconducting metals in the extreme anomalous limit (penetration depth \ll coherence length).

The value of the critical temperature for all samples except one agreed with the literature value within uncertainty limits. The model did not give good quantitative agreement with the observed spectra but did give qualitative features which agreed with the observed spectra.

Dedication

To the memory of my late mother, Carol Ann Geiger

Quotation

Nam si tantundemst in lanae glomere quantum
corporis in plumbo est, tantundem pendere par
est...

Lucretius, De Rerum Natura, 1.360-361

Acknowledgement

I would like first to thank my Senior Supervisor Professor B. P. Clayman for the support he has given me during my time at Simon Fraser University. I would also especially like to thank Professor S. Gygax and coworkers for performing the critical temperature measurements. I would like to thank Professor A. E. Curzon and coworkers for the scanning electron microscope measurements. I would like to thank Professor E. D. Crozier for the use of his evaporator for preparing the samples. I would like to acknowledge two fellow graduate students, Messrs. A. G. Steele and W. G. McMullan, for their many interesting discussions.

Table of Contents

Chapter	Page
1. Introduction and Historical Background.....	1
A. History of far-infrared spectroscopy of lead thin films.....	1
B. Original motivation for this research.....	6
2. Sample Preparation.....	7
3. Sample Characterization Procedures and Results and FIR Measurement Procedures.....	12
A. Introduction.....	12
B. DC Resistance Measurements.....	12
C. Shielding Effect Measurement.....	19
D. Summary of critical temperature measurements...	20
E. Microstructure Examination.....	24
F. FIR Transmission Measurements.....	30
4. Infrared Results and Analysis.....	40
A. Observations and Hypothesis.....	40
B. Wave Guide Theory.....	50
C. Composite Material.....	55
D. Modelling the FIR Data.....	56
E. Models used to describe transmission through the grains.....	59
F. Models used to describe transmission through a "wave guide".....	61
G. Fitting the data.....	63

Chapter	Page
4. Infrared Results and Analysis	
H. Fitting procedure and observations.....	64
I. Evaluation of model and discussion of results..	67
J. Relation of the model parameters to sample characterization.....	68
5. Conclusion.....	71
A. Summary.....	71
B. Future Experiments.....	71
6. Appendix.....	73
A. Calculation of Uncertainties.....	73
7. List of References.....	75

List of Tables

Table	Page
1. DC Resistance Critical Temperature Values.....	14
2. Representative Wave Guide Dimensions.....	24
3. Attenuation Constants for Perfectly Conducting Walls..	54
4. Attenuation Constants for Finite Conducting Walls.....	54
5. Fitting Parameters for Transmission Ratio Plots.....	66
6. Ratio of Gap Energy to Critical Temperature Values....	70

List of Figures

Figure	Page
1. Schematic for DC Resistance Electronics.....	16
2. Resistance vs. Temperature for Pb2.....	18
3. Magnetization vs. Temperature for Pb1.....	23
4. Electron Microscope Photograph of Pb3 and.....	26
5. Electron Microscope Photograph of Pb4.....	28
6. Thermal and Sample Stage Assembly.....	32
7. Transmission vs. Wavenumber for Pb4 and Pb5.....	39
8. Complex Conductivity, Transmission Ratio, and Surface Resistance Ratio.....	42
9. Observed Transmission Ratios for Pb1 and Pb2.....	45
10. Observed Transmission Ratios for Pb3 and Pb4.....	47
11. Observed Transmission Ratios for Pb5 and Pb6.....	49
12. Diagrammatic Representations for the Model Film.....	58

Chapter 1: Introduction and Historical Background

The subject of this thesis concerns the measurement of the superconducting energy gap of contaminated lead films using the experimental techniques of far-infrared spectroscopy. Measurements of the superconducting critical temperature were also performed and the results of which are included in this thesis. The ratio of

$$\frac{2\Delta(T=0)}{k_B T_C}$$

where Δ is the superconducting energy gap, k_B is the Boltzmann constant and T_C is the critical temperature, provides a measure of the electron-phonon coupling strength.

A. History of far-infrared spectroscopy of lead thin films

The theory developed by Bardeen, Cooper, and Schrieffer¹ hereafter referred to as BCS theory introduced an energy gap parameter to describe the pairing of electrons in the ground state. The gap energy is the minimum energy needed to split a pair of electrons and to cause them to behave as "normal" electrons. The excitation energy can be either thermal or electromagnetic in nature. The gap is largest at $T=0$ and decreases to zero at the critical temperature.

The foundations of far infrared spectroscopy on superconducting materials were developed by Tinkham and coworkers²⁻⁵. The majority of the work involved transmission and reflection measurements on thin films except for the work of Richards and Tinkham⁴ which measured the energy gap in bulk samples. From the transmission and reflection data, Tinkham and coworkers developed methods to calculate the real and imaginary parts of the complex conductivity. This author adopts the convention of Ginsberg and Tinkham³ and the convention of Carr⁶ et. al. in defining the complex conductivity as

$$\sigma(\omega) = \sigma_1 + i\sigma_2 \quad (1-1)$$

with a time dependence of the electromagnetic field of the form

$$e^{-i\omega t}$$

The complex conductivity is related to the complex dielectric function by

$$\epsilon(\omega) = \epsilon_\infty + \frac{4\pi i}{\omega} \sigma(\omega) \quad (1-2)$$

It is from the complex dielectric function that the optical properties, such as the absorption coefficient, can be calculated. The real and imaginary parts of the complex

conductivity are related to each other by the Kramers-Kronig⁷ relations

$$\sigma_1(\omega) = \frac{1}{\pi} \int_{-\infty}^{\infty} \frac{\omega' \sigma_2(\omega') d\omega'}{\omega'^2 - \omega^2} + C \quad (1-3)$$

$$\sigma_2(\omega) = \frac{-\omega}{\pi} \int_{-\infty}^{\infty} \frac{\sigma_1(\omega') d\omega'}{\omega'^2 - \omega^2} \quad (1-4)$$

Mattis and Bardeen⁸ have derived expressions based on BCS theory for the real and imaginary parts of the complex conductivity for both normal and superconducting metals in the extreme anomalous limit. Good agreement above the energy gap was obtained between the experimentally determined complex conductivity of Glover and Tinkham² and Palmer and Tinkham⁵ and the expressions derived by Mattis and Bardeen. However, Ginsberg and Tinkham³ and Richards and Tinkham⁴ saw evidence of a precursor structure below the energy gap in the real part of the complex conductivity. According to the Mattis and Bardeen calculation at $T=0$, the real part of the complex conductivity is infinite at zero frequency and zero at finite values for the frequency below the gap frequency. The precursor structure suggests that there are absorptive processes within the energy gap.

Palmer and Tinkham tried to determine details of this

17
precursor but found no experimental evidence of a precursor of the magnitude reported by Ginsberg and Tinkham. Nam⁹ calculated the energy gap for lead in the strong coupling case and found good agreement with the value of the energy gap measured by Palmer and Tinkham.

More recent work on far-infrared spectroscopy of superconducting films has been performed by Carr¹⁰ et al. who observed anomalous behavior of their lead films. They observed enhanced absorption compared with the prediction of BCS in the superconducting state at frequencies around and just below the gap frequency. They interpret the enhanced absorption as indicating that the real part of the complex conductivity for the superconducting state is greater than the real part of the complex conductivity for the normal state. The enhanced absorption was limited to films with DC sheet resistances greater than 50 ohms-per-square. For films with lower sheet resistance (greater thickness), ordinary BCS behavior was observed.

The superconducting energy gap of bulk metals and alloys was measured by Richards and Tinkham⁴ and by Leslie and Ginsberg¹¹ using far-infrared radiation incident on non-resonant superconducting cavities. They determined their absorption edges above the energy gap from the difference between the surface resistance of the cavity

in the normal state and the superconducting state. Both Richards and Tinkham and Leslie and Ginsberg observed that the onset for absorption as predicted by Mattis and Bardeen was much more gradual than their experimentally observed absorption edges.

In the superconducting state, the extreme anomalous limit is valid only if the penetration depth is much less than the coherence length. This is known as the Pippard limit. If the coherence length is much less than the penetration depth then the corresponding limit is the London limit. Also for superconductors, if the mean free path is not much greater than the coherence length then the superconductor can be called a "dirty" superconductor.

The BCS value for the coherence length for lead³⁷ is 830 Angstroms. The observed value for the London penetration depth at $T=0$ K for lead³⁷ is 390 Angstroms. Hence, the ratio of the coherence length to the penetration depth for lead is approximately 2.1. Although lead does not strictly satisfy the condition for use of the extreme anomalous case, the use of the extreme anomalous limit should be more nearly valid than the use of the London limit.

One need not be confined to the extreme anomalous limit in order to calculate the complex conductivity.

Leplae¹² writes the real part of the complex conductivity

for a superconductor in terms of the normal state conductivity and uses the Kramers-Kronig relation in order to calculate the imaginary part of the complex conductivity. If one assumes that the normal state conductivity is constant, the Mattis Bardeen anomalous limit is returned. Another form for the normal state conductivity would be the Drude form

$$\sigma_N(\omega) = \frac{\sigma_0}{(1 - i\omega\tau)} \quad (1-5)$$

Karecki¹³ et. al. have used this procedure for modelling their data on the far-infrared transmission of the strongly coupled superconducting NbN thin films.

B. Original motivation for this research

Dynes and Rowell¹⁴ performed tunnelling measurements on lead and lead-bismuth alloy thin films in order to determine the energy gap. We were interested in comparing the energy gap value of Dynes and Rowell with that determined by far-infrared spectroscopy. Then we attempted to grow, characterize, and measure spectroscopically thin films of lead-bismuth alloys with the goal of determining the superconducting energy gap. It was found however that the unalloyed lead films that we were growing as a starting point warranted sufficient need of investigation so as to compose the research of this thesis.

Chapter 2: Sample Preparation

The films were deposited by thermal evaporation of pure lead from a tungsten boat. The typical pressure inside the evaporator was 2×10^{-6} torr during the evaporation. The pressure was measured with a vacuum ionization gauge¹⁷. The thickness of the sample was measured using a digital thickness monitor¹⁸ which employed a water-cooled quartz crystal.

The substrates used were fire-polished sapphire platelets for the critical temperature measurements and wedge-cut sapphire discs for the optical measurements. The sapphire platelets were approximately 1 cm^2 in area and had their corners removed in order to facilitate their mounting for the critical temperature measurements. The sapphire discs were $1/2$ inch in diameter.

At this point this author cannot stress enough the importance of substrate preparation and substrate temperature during the evaporation on the film quality. A film of high quality can be viewed as satisfying two criteria:

- a) the film should be electrically conductive:
- b) the film should have a thickness which is comparable to the skin depth.

If the film is thicker, transmission measurements become

impossible. It was found that high quality films were free of large microcrystals. The large microcrystals tended to give the film a cloudy appearance as opposed to a shiny appearance. It was also found that high quality films was composed of many small (on the order of a micron) grains.

The cleanliness of the substrate was found to have a profound effect on the quality of the film. This author adopted the guidelines from "Thin Film Processes"¹⁵ concerning the chemical etching of insulators and dielectrics. In summary, the sapphire wedge-cut discs and sapphire fire-polished platelets were first ultrasonically cleaned in acetone and then in ethanol in order to remove organic impurities. The substrates were then boiled in aqua regia and then in a mixture of 85% phosphoric acid and 15% sulphuric acid. The aqua regia cleaned the substrates of any residual lead that remained after the recycling of the substrates. The phosphoric acid and sulphuric acid mixture slowly etched the sapphire surface. The goal was not to produce a surface suitable for epitaxial growth, but to maintain a high degree of cleanliness nonetheless. The substrates were then rinsed several times in distilled water and then stored in ethanol in a glass beaker covered with aluminum foil. The substrates were dried in dry nitrogen before being mounted.

A copper sample holder, which was part of the optical

assembly for the cryostat insert, was used to hold the substrates in the evaporator. This lessened the risk that the optical sample would be damaged when the films were transferred from the evaporator to the cryostat. The wedge-cut disc of sapphire, which served as the optical substrate, was mounted into the optical path of copper sample holder. Mounted onto the sample holder next to the optical substrate, but not shadowing it, were two sapphire platelets. The platelets were used for the critical temperature measurements.

The sample holder was placed in the evaporator and was placed in good thermal contact with the water cooled mount. It was necessary to cool the mount because of the high mobility of lead atoms at temperatures that would be experienced during the evaporation process. The vapor temperature¹⁶ for lead is 700 Celsius at 1×10^{-6} Torr. If the substrates were not cooled, they would be radiatively heated from the boat and lead atoms would tend to form microcrystals. This is due to the preference of lead atoms to attach to lead rather than the substrate. Controlling the temperature of the substrates during the evaporation allowed films to be made which were free of microcrystals and had a uniform thickness.

The boat was heated with an AC power supply. A shutter or vane was in place during the initial heating to

protect the substrates. After approximately 50 Angstroms of lead had been evaporated onto the vane, the vane was moved, the thickness monitor was quickly reset and the film deposited onto the substrates. The rate of evaporation was controlled by the current through the tungsten boat. The current was increased after the vane was removed in order to evaporate quickly. This was necessary because lead is a good getter while in the vapor state. The time elapsed during the evaporation was approximately 30 seconds. The current was turned down before the desired thickness was reached, to anticipate the slow thermal response of the tungsten boat.

After the evaporation was completed, the evaporator was backfilled with nitrogen gas and the sample holder was removed and the sapphire platelets were removed. The sapphire platelets were usually stored in air and later transferred to another room where the critical temperature measurement was performed. The sample holder with the optical substrate was then mounted onto the cryostat insert. The cryostat insert was then placed into the cryostat sample chamber and the sample chamber pumped out. The sample chamber with the optical sample was kept under vacuum from this point onward.

Many evaporations were performed in order to obtain high quality films. Some problems that were experienced

were shadowing effects of the sample holder on the optical substrate, formation of visible pinholes in the film, and overshooting the desired thickness by evaporating too quickly or not anticipating the thermal response of the boat properly. During the course of the research we ended up with six samples, designated Pb1-Pb6, that were well characterized and whose optical properties were measured.

Chapter 3: Sample Characterization Procedures and Results and FIR Measurement Procedures

A. Introduction

Sample characterization involved determination of the critical temperature and examination of the film microstructure. Two methods were employed to determine the critical temperature; the first was a four-probe DC resistance measurement and the second was a shielding measurement. The critical temperature measurements were performed by S. Gyax and coworkers. The microstructure was examined with a scanning electron microscope. A. E. Curzon and coworkers performed the microscopic examination. This author would like to express his gratitude to these two research groups for their time and efforts.

Far-infrared spectra were obtained by measuring the transmission through the lead films in both the superconducting and normal states over the energy range of 5 to 100 cm^{-1} . Transmission in the superconducting state was divided by transmission in the normal state to yield the energy response of the superconducting lead films.

B. DC Resistance Measurements

Evaporated lead films were deposited on the sapphire platelets as described in Chapter 2. The platelets were

mounted on the copper tip of a thin walled stainless steel probe using Apiezon grease which supplied the thermal link between the platelets and the probe. Four short Formel wires of 0.0031 inch diameter were stripped with Strip-X and were attached directly to the film using silver DAG. These four wires were generally attached at the corners of a square geometry. The platelets were originally 1 cm^2 in area but had their corners removed so that the platelets would fit on the end of the probe. The four wires were then soldered to wires that travel the length of the probe; two act as current source wires and two as voltage leads. A calibrated thermal resistor¹⁹, which is in good thermal contact with the copper tip, was used to monitor the sample temperature. The probe was then connected to the supporting electronics, shown schematically in Figure 1. The probe is then inserted into a closed cycle Helium⁴ refrigerator²⁰.

As the probe was slowly lowered into the closed cycle refrigerator, a plot of resistance versus temperature was obtained. Figure 2 shows one such plot. By raising and lowering the probe while in the vicinity of the critical temperature, the temperature immediately before the sharp drop in resistance, T_{C1} , and the temperature corresponding to the first point where zero resistance is noted, T_{C2} , can be determined. These values, listed in

Table 1 for the five of the six films measured spectroscopically, give a measure of the sharpness of the superconducting transition. The average of T_{c1} and T_{c2} was taken to be the superconducting transition temperature. The ratio of the resistance of the film at 300 K to the resistance at 10 K (known as the residual resistance ratio or RRR) is given in Table 1. From the residual resistance ratio the mean free path was calculated. This was done by multiplying the literature value for the room temperature conductivity of lead by the residual resistance ratio in order to obtain the conductivity of the film at 10 K. The conductivity at 10 K is then divided by the ratio³⁸ of the conductivity to the mean free path in order to obtain the mean free path. The uncertainty calculations are described in detail in Appendix A.

Table 1

DC Resistance Critical Temperature Values

SAMPLE	T_{c1}	T_{c2}	T_c	ΔT	RRR	ΔRRR	m.f.p.
Pb2	7.15K	7.20K	7.18K	.03K			
Pb3	7.15K	7.20K	7.18K	.05K	12.4	1.4	636 A
Pb4	7.30K	7.35K	7.33K	.03K			
Pb5	7.00K	7.30K	7.15K	.20K	15.1	0.4	775 A
Pb6	7.25K	7.40K	7.33K	.13K	11.7	2.2	600 A

Figure 1

Schematic for the supporting electronics used for the DC resistance measurements. BDC = Binary to Decimal Converter. CCS = Constant Current Supply. DMM = Digital Multimeter.

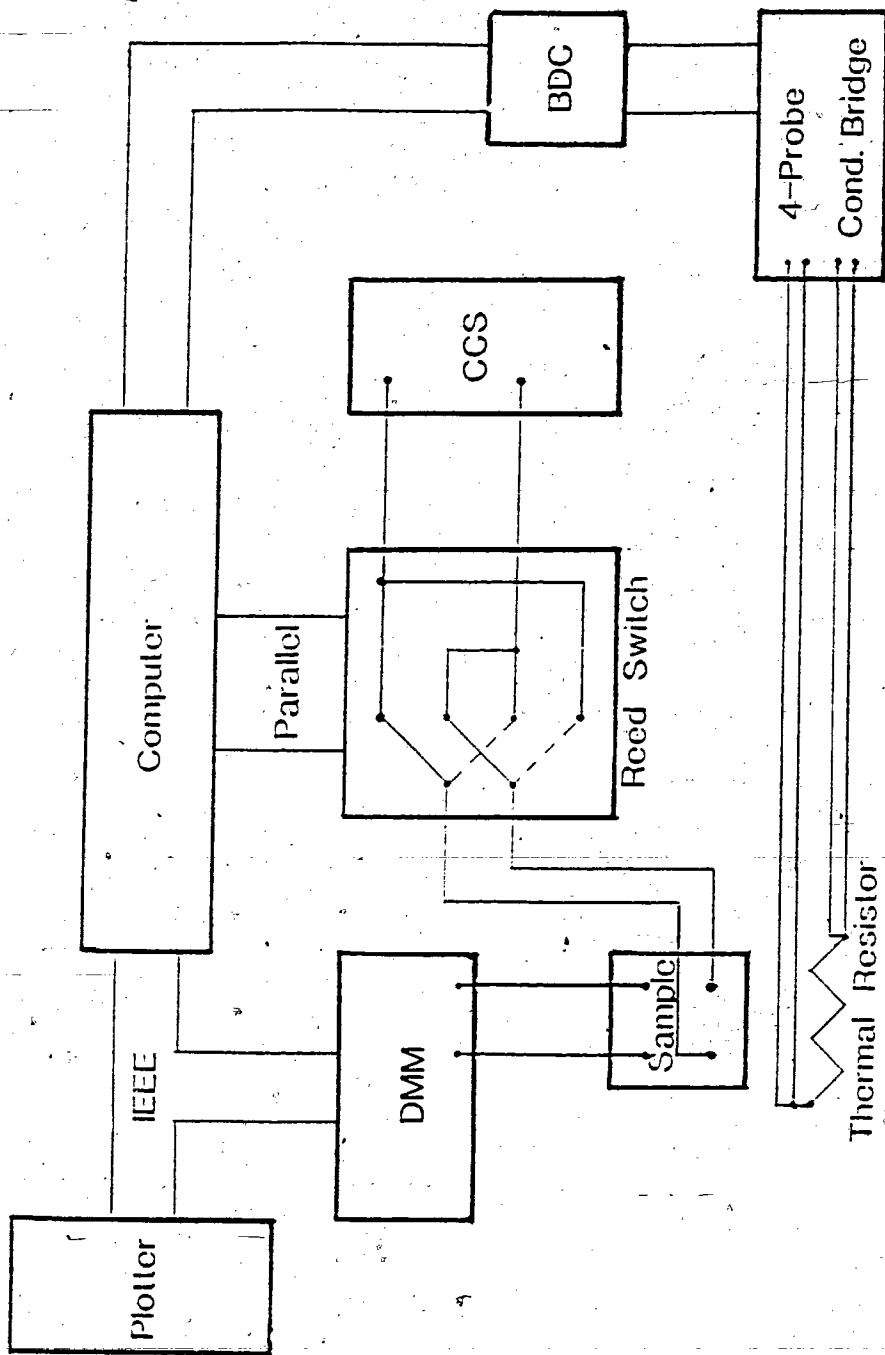


Figure 1

Figure 2

Resistance plotted against temperature for sample Pb2. Inset shows sharpness of the superconducting transition.

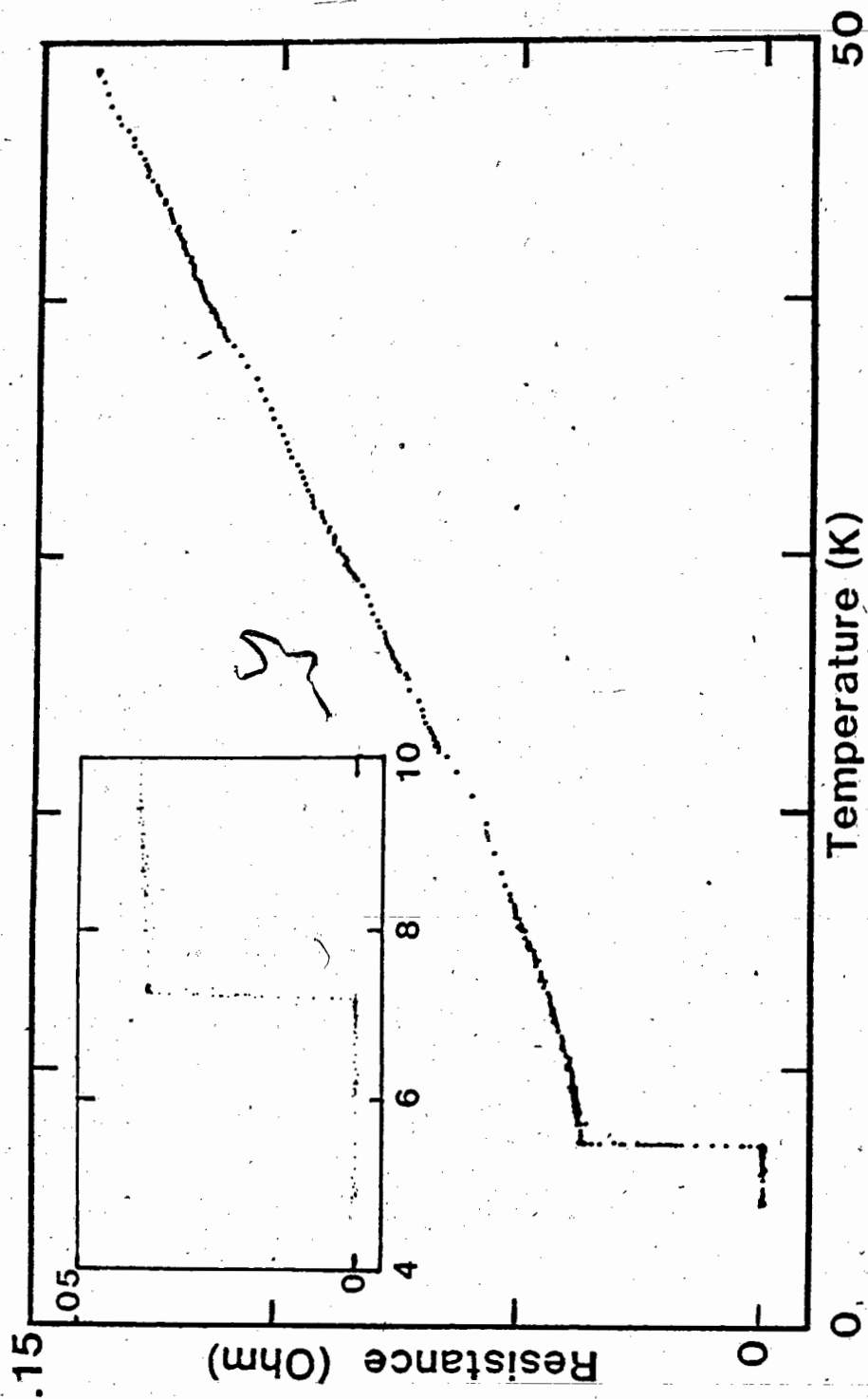


Figure 2

C. Shielding Effect Measurement

The measurement of the superconducting transition temperature by means of the shielding effect was performed on a lead film (designated as Pb1) that was evaporated onto a small piece of a sapphire platelet that was identical to the platelet used for the DC resistance measurement. The details of the apparatus and its operation are described elsewhere²¹.

In summary, the sapphire platelet was mounted onto a sapphire tipped probe using Apiezon grease with the film side against the probe. A small piece of niobium wire²² was mounted along the side of the sapphire tip, running parallel along the length of the sapphire. The probe was then placed in a He⁴ cryostat which contained a SQUID magnetometer system. The sample was cooled in zero field to 4.2 K, a small DC magnetic field was applied and the sample was heated by applying a current to the heating wire within the probe. The changes in magnetization of the lead sample and the niobium reference were monitored as they went from the superconducting (Meissner) state to the normal state. The magnetic field was removed when the sample and reference were in the normal state and both were allowed to cool again in zero field. This cycle was repeated three times.

The SQUID output showed two distinct steps, corresponding to the magnetic flux lines first entering the lead film and then the niobium wire. Figure 3 shows the magnetization as a function of temperature for the lead film, corresponding to the optical sample Pb1 in Table 2, and the niobium reference. Figure 3 represents the average of four magnetization cycles. The midpoint of the change in magnetization for the niobium wire was measured to be $8.90 \pm .08$ K. The midpoint in the change of magnetization for the lead film was $7.11 \pm .08$ K. Details of the uncertainty calculations are presented in Appendix A.

D. Summary of critical temperature measurements

The literature value for the critical temperature for bulk lead³⁵ is 7.26 K. A more recent value for critical temperature for bulk lead³⁶ is 7.196 ± 0.006 K. The literature value for the critical temperature of lead thin films¹⁴ is 7.20 K. The lead films in Reference 14 were evaporated onto an aluminum oxide layer that had formed on a previously evaporated aluminum film. The aluminum film was evaporated onto a glass substrate. Only sample Pb4 did not agree with the latest literature value for bulk lead within uncertainty limits. All of the samples were clustered around each other to within 0.22 K. The value of the critical temperature by the DC resistance measurement did agree within uncertainty limits with the

value of the critical temperature as measured by the change in magnetization except for samples Pb4 and Pb6.

The literature value for the critical temperature for bulk niobium³⁶ is 9.25 ± 0.02 K. The measured critical temperature of niobium did not agree within uncertainty limits. It was in fact too low by 0.35 K. This may have been due to a calibration error in the thermal resistor or due to a problem with the niobium itself. A problem with the thermal resistor may explain why sample Pb1 registered the lowest critical temperature. Yet Pb1 still agreed with the literature value within uncertainty limits.

The values of the residual resistance ratio that was measured for two of the three samples, Pb3 and Pb6, agreed with each other within uncertainty limits. The value of the residual resistance ratio for sample Pb5 did not agree with either of the other two samples but was very similar. Since the residual resistance ratio is a convenient approximate indicator of sample purity, it was concluded that the three samples whose RRR was measured had an approximately equivalent degree of contamination.

Figure 3

Magnetization plotted against temperature for sample Pb1 and for the niobium wire. Sample was cooled in zero field and then warmed in a small DC field. The low temperature tail is related to the penetration depth of the field.

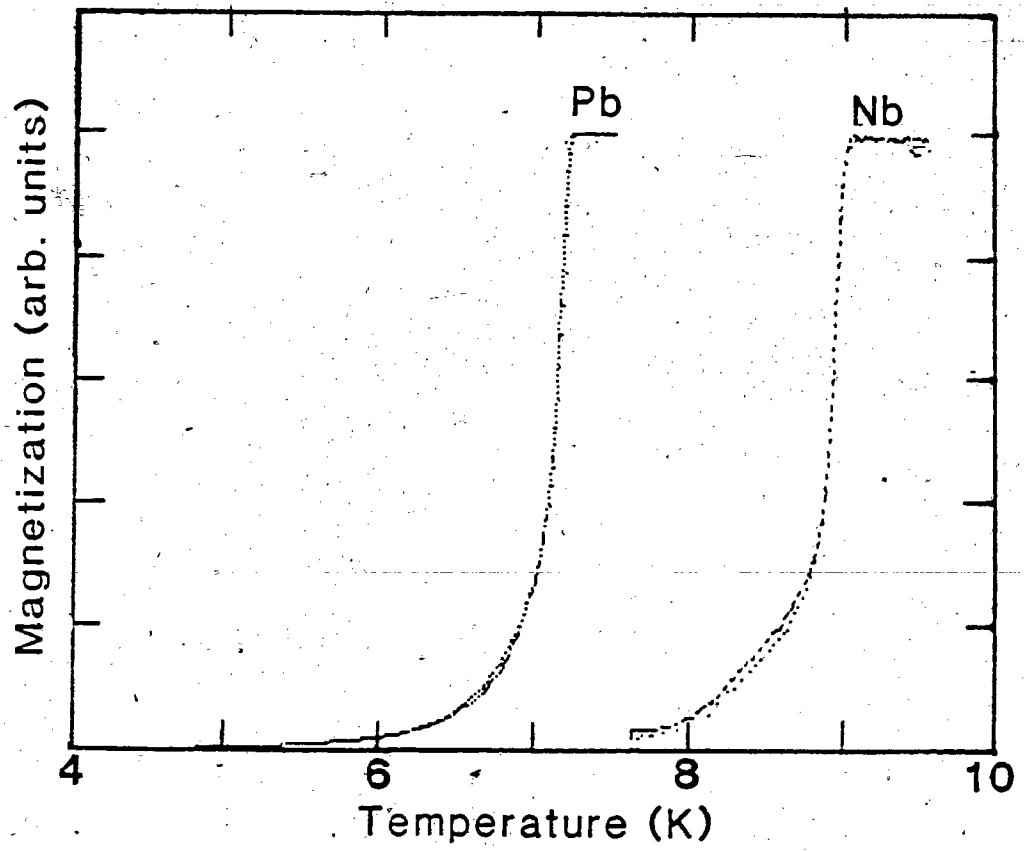


Figure 3

E. Microstructure Examination

Figure 4 and Figure 5 show photographs of two different lead films that were examined under a scanning electron microscope²³. The purpose of the examination was to determine the granularity of the films. Table 2 gives the thickness, measured during the evaporation, of the six samples that were measured optically and gives representative dimensions for the spaces between grains for the two samples that were measured under the scanning electron microscope. The dimension a is the width of a gap between grains and b is the length of a gap. These values will be important for the wave guide analysis in the next chapter.

Table 2

Representative Wave Guide Dimensions

Sample	Thickness	a (nm)	b (nm)
Pb1	59.0 nm		
Pb2	50.5 nm		
Pb3	43.5 nm	120	1,560
Pb4	49.0 nm	230	1,110
Pb5	46.0 nm		
Pb6	49.0 nm		

Figure 4

Top: Scanning electron microscope photograph of sample Pb3. Black bar corresponds to 953 nm. Applied voltage was 14 kV. Magnification was 10.49 kX.

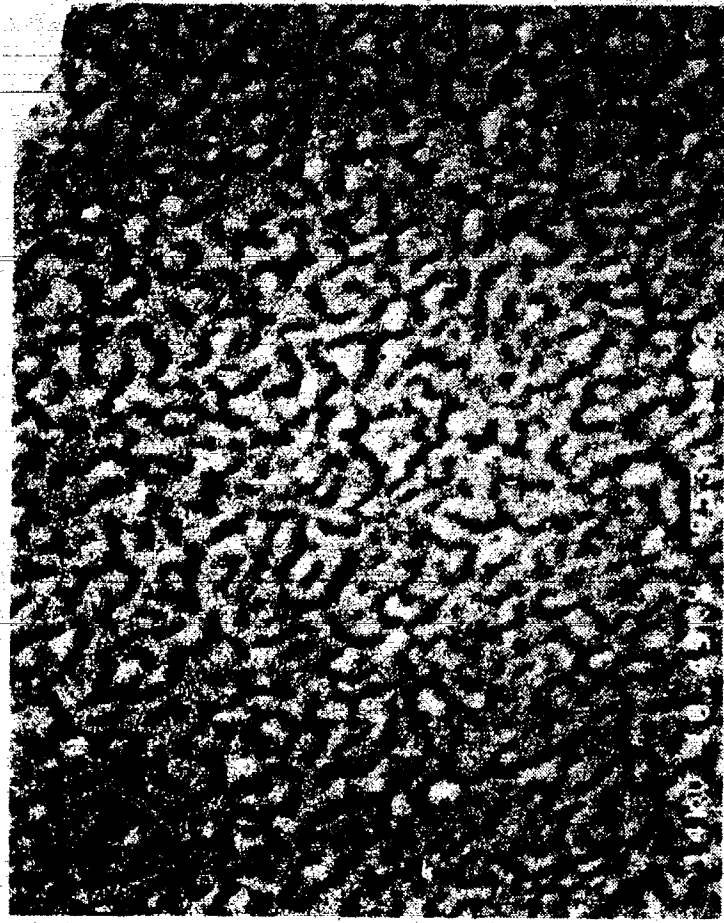


Figure 4

Figure 5

Bottom: Scanning electron microscope photograph of sample Pb4. White bar at the bottom corresponds to 1030 nm. Applied voltage was 25 kV. Magnification was 9.69 kX.

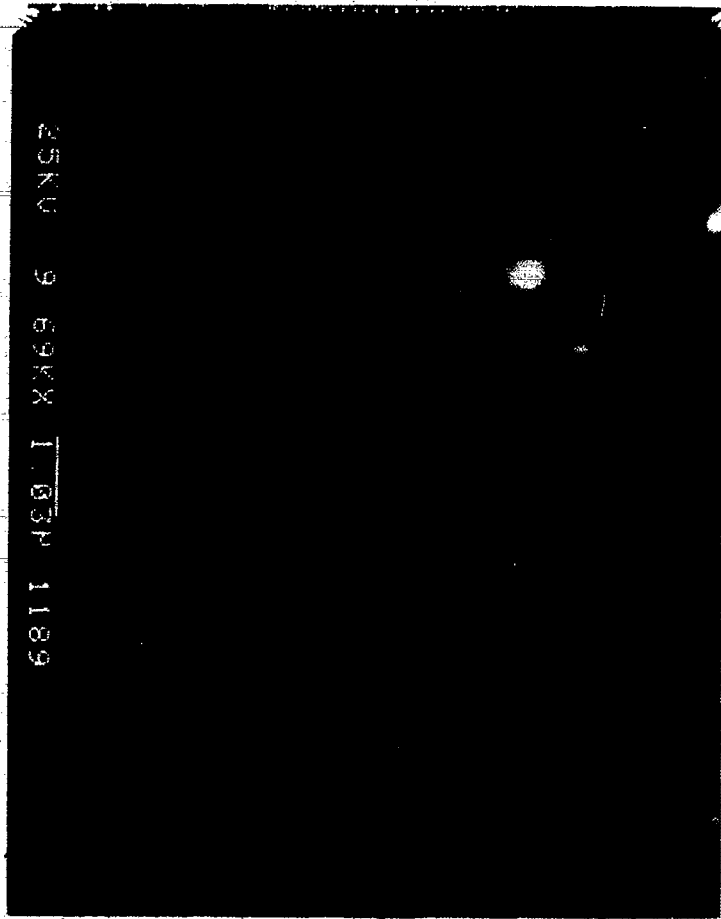


Figure 5

By comparing the values for the mean free path presented in Table 1 with the size of the grains, it was concluded that the scattering of the electrons occurs mostly within the grain before the electrons reach the grain boundary. By comparing the values for the mean free path with the thicknesses of the film presented in Table 2, it was concluded that there may be a contribution to the conductivity due to the scattering of electrons at the surface of the film.

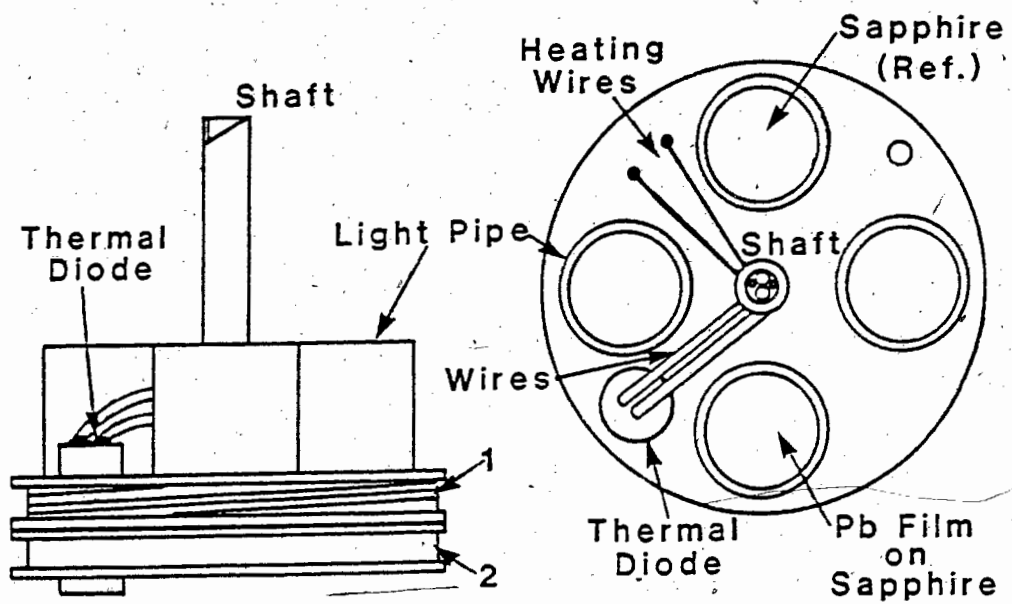
F. FIR Transmission Measurements

In the previous chapter, the handling of the copper sample holder was briefly discussed. A more thorough discussion follows. The copper sample holder was attached to the thermal control stage which was a similar copper disc which contained the heater²⁴ and the thermal diode²⁵. Figure 6 shows how the two discs (stages) are arranged. This design allowed the optical sample to be mounted in such a way as to minimize the risk of damage. Thin brass rings approximately 0.0312 inch thick with an outer diameter of 0.500 inch and an inner diameter of approximately 0.437 inch were placed on the sample and on the reference to block out any far-infrared radiation that might leak around the edges of the sample.

The two stages were then enclosed inside a brass can that included a feedthrough which allowed the stage assembly to be rotated from outside the cryostat. The brass can was coupled to the interferometer and to the detector by means of 0.500 inch inner diameter brass light pipe. At the interferometer end of the light pipe, black polyethylene was used to form a vacuum window and to block out the visible components of the far-infrared source. Within the light pipe that coupled the sample stages to the detector section was a 0.500 inch diameter, wedge shaped LiF crystal held in place with rings made from stainless

Figure 6

Side view and top view of the thermal and sample stages joined together. Heater wire wrap around the thermal control stage after entering from the top. Diameter of the stage assembly is approximately 4.3 cm.



1-Thermal Control Stage

2-Sample Holder Stage

Figure 6

steel tube. The LiF crystal acted as a cold filter to block out radiation at energies higher than approximately 220 cm^{-1} .

The cryostat that was used served to cool the sample and to contain a He^3 bolometer that was used to detect the far-infrared radiation transmitted through the sample. The details of the cryostat along with the details of its operation are described elsewhere.^{26,27} In summary, the cryostat is a He^4 immersion dewar with a one shot He^3 refrigerator that is used to cool a composite germanium bolometer that operates at 0.4 K. The sample section is coupled to the He^4 bath via exchange gas and is optically connected to the detector via a tapered brass light pipe. A Mylar window provides the vacuum isolation between the sample section and the detector section. The He^4 bath can be placed under vacuum and can be kept in a superfluid state for up to ten hours.

The modulation of the far-infrared radiation was accomplished by a Michelson interferometer²⁸ for several experiments and by a lamellar interferometer²⁹ for several other experiments. The interferometers were controlled by an IBM PC compatible microcomputer. Details of the interferometer operation and its computer interfacing are described elsewhere³⁰. The computer also functioned as the collection port for the data generated by

the detector electronics and performed the necessary Fourier transforms.

The Michelson interferometer and the lamellar interferometer employ a mercury lamp as the source of the far-infrared radiation. The Michelson interferometer operates on the principle of amplitude division while the lamellar interferometer operates on the principle of wave front division³¹. After their respective division, both interferometers introduce an optical path difference, Δ , before recombining the divided radiation. The Michelson interferometer accomplishes the amplitude division by using a Mylar beam splitter. The path difference is introduced by using separate mirrors for each path, one fixed and one allowed to move. The lamellar interferometer divides the wave front and presents an optical path difference by the motion of one lamellar grating with respect to a fixed grating.

The radiation intensity that reaches the detector is expressed mathematically by

$$I(\Delta) = \int_0^{\infty} S(\nu)(1 + \cos 2\pi\nu\Delta) d\nu \quad (3-1)$$

where Δ is the optical path difference and ν is the frequency of the far-infrared radiation, measured in cm^{-1} . $S(\nu)$ is the intensity distribution, as a function of frequency, that reaches the detector. By changing the

path difference between the wave front in incremental steps and measuring the intensity of radiation transmitted through the sample at each step, a distribution of intensity, $I(\Delta)$, is obtained. This distribution of intensity is then Fourier transformed in order to obtain the frequency response $S(\nu)$ of the sample. $I(\Delta)$ is the Fourier transform of the desired energy spectrum, $S(\nu)$.

The transmission spectra were obtained through the following procedure. The samples were cooled to approximately 2 K which placed the film in the superconducting state, well below the superconducting transition temperature (approx. 7 K). The interferometer was set up to cover a specific frequency range for a specific resolution. Typical values of 100 cm^{-1} for the cutoff frequency and 4 cm^{-1} for the resolution were used. Room temperature filters were used to insure that frequencies higher than approximately 85 cm^{-1} would be blocked.

At each incremental step corresponding to a specific path difference, signal was measured with a lock-in amplifier. The incident radiation was chopped at a frequency of 30 Hz. The bolometer was in series with a 7 MOhm resistor, which was in the cryostat. This series combination formed a voltage divider circuit and was driven by an external battery-powered source. The applied voltage

was approximately 7.5 volts. The bolometer AC output was then sent to the lock-in amplifier. The DC output of the bolometer could also be monitored in order to assist in sample alignment and to determine if there were any heating effects due to large amounts of radiation incident on the bolometer.

The output of the lock-in amplifier was sent to both a chart recorder and to an analog to digital converter (ADC). The gate time on the ADC was usually 5 seconds if the signal was strong and up to 12 seconds if the signal was weak. As the interferometer passed through the zero path difference point, a peak in the intensity was observed. The total distribution of the intensity at the bolometer, $I(\Delta)$, is known as an interferogram. Each interferogram was stored in the computer and was individually Fourier transformed. The resultant spectra were then averaged together for several scans of the sample in the superconducting state.

The sample was then driven into the normal state by applying a small current of approximately 0.3 mA to the heater²⁴ (17.44 ohms) that was in good thermal contact with the sample stage assembly. The temperature corresponding to the normal state was approximately 10 K. A corresponding drop in signal was observed on the chart recorder output which was due to the sample becoming less

transparent in the normal state. Any exchange gas in the sample chamber was pumped out in order to avoid excess liquid helium boil-off. The data for the normal state was handled in the same way as the superconducting state data. Figure 7 shows two averaged spectra for both the superconducting state, T_S , and the normal state, T_N .

The ratio of T_S to T_N was performed digitally. This is also shown in Figure 7. The noise in the T_S/T_N spectra at high and low energy results from the division of low intensity for the superconducting state by low intensity for the normal state. The plots in Figure 7 represent typical spectra that were observed during the course of the experiments. These ratios and the ratios corresponding to the remainder of the samples will be presented in the following chapter.

Figure 7

Top: Superconducting and normal state transmission plotted versus wavenumber for sample Pb4.

Chaindotted line is the T_S/T_N ratio. Arrows show instrument resolution (4.05 cm^{-1}).

Bottom: Same for sample Pb5.

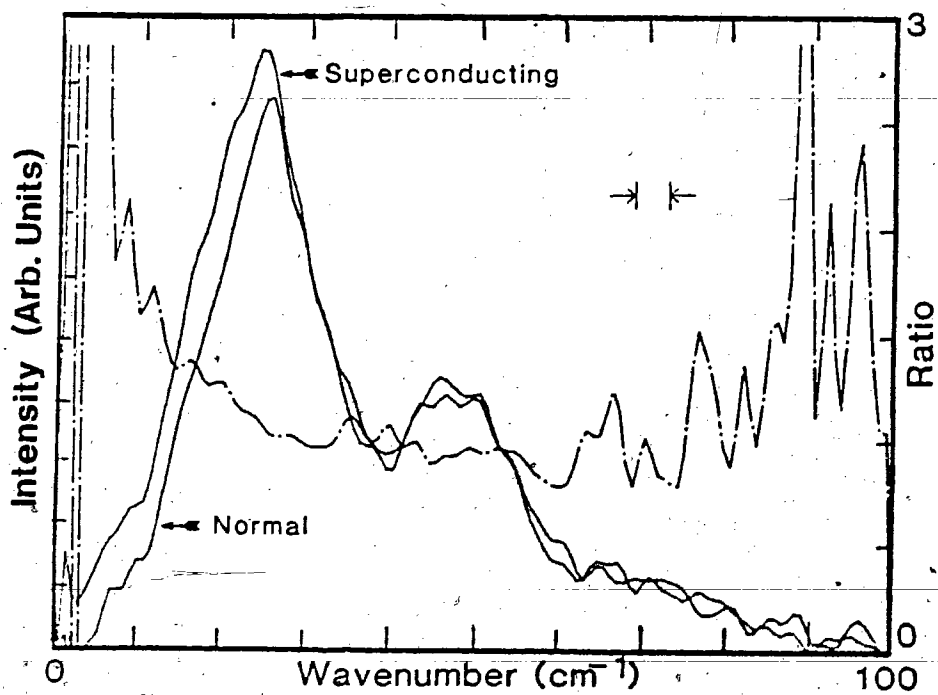
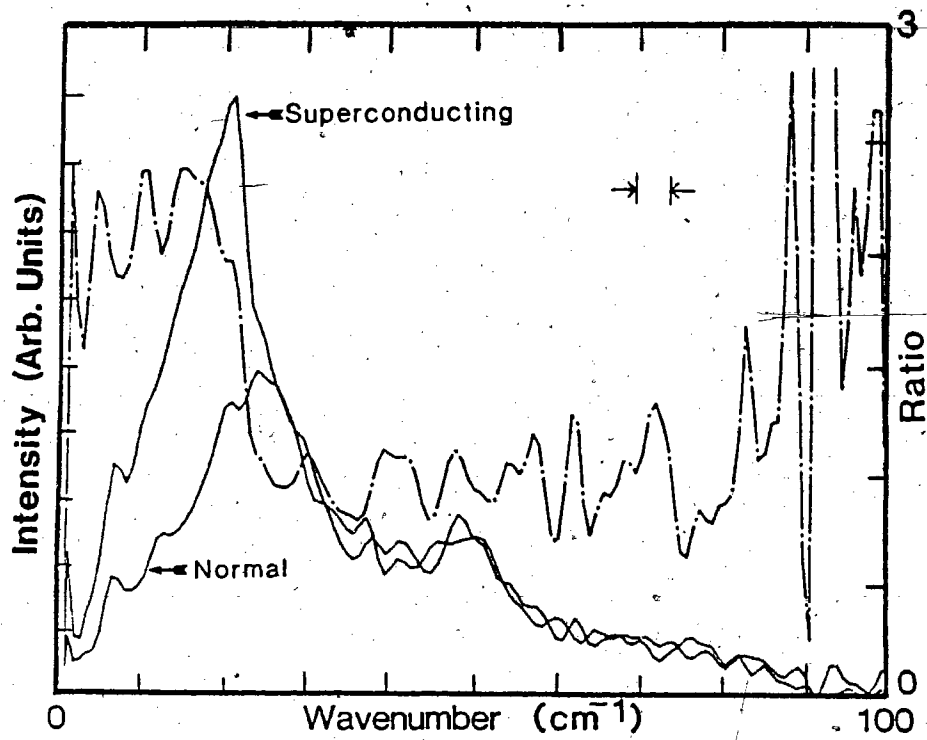


Figure 7

Chapter 4: Infrared Results and Analysis

A. Observations and Hypothesis

As stated in Chapter 1, Mattis and Bardeen⁸ derived expressions based on BCS theory for the real and imaginary parts of the complex conductivity for both superconducting and normal metals in the extreme anomalous limit. Figure 8 shows the calculated complex conductivity at $T=0$ K; the details of these calculations will be presented later in this chapter. Glover and Tinkham² have derived an expression to calculate the T_S/T_N ratio as a function of the real and imaginary parts of the complex conductivity and as a function of the normal state transmission. Figure 8 also shows the T_S/T_N ratio calculated using the Mattis and Bardeen expressions for the real and imaginary parts of the complex conductivity.

There are two distinct features of the theoretical T_S/T_N ratio which were used as a basis of comparison with the experimentally observed ratios. The first is that the theoretical ratio approaches zero at zero energy. According to the Mattis and Bardeen calculation, the film would be perfectly reflecting at zero energy. This is due to the existence of a delta function in the real part of the complex conductivity at zero energy, corresponding to infinite DC conductivity. This is in qualitative

Figure 8

Top: The real and imaginary parts of the complex conductivity as a function of reduced frequency. Also shown is the T_S/T_N ratio calculated for a normal state sheet resistance of 228 ohms per square ($T_N=0.5$).

Bottom: Ratio of the superconducting to normal surface resistance as a function of reduced frequency. The same values for the real and imaginary parts of the complex conductivity that were used to calculate T_S/T_N were used here.

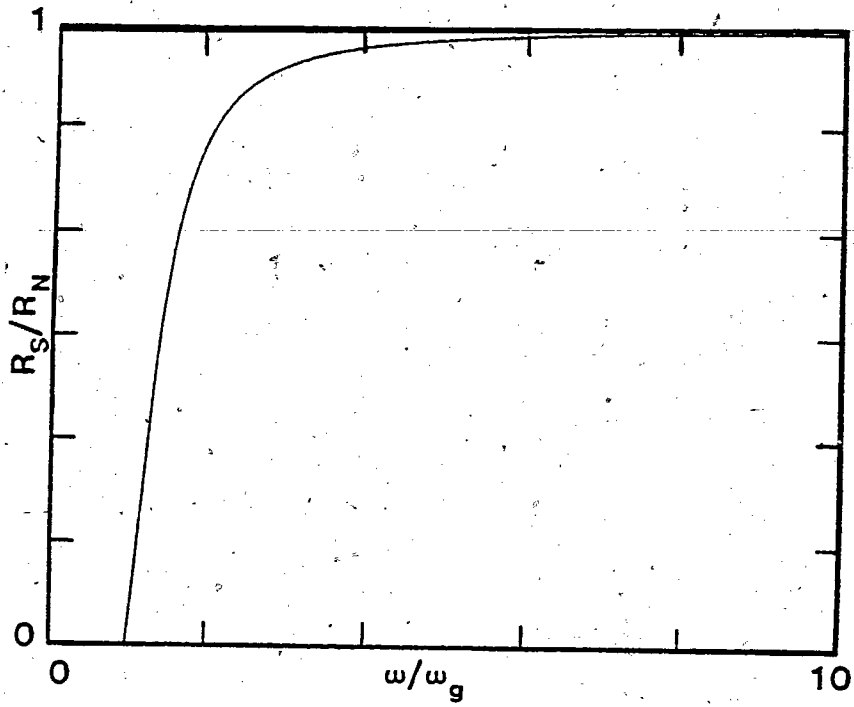
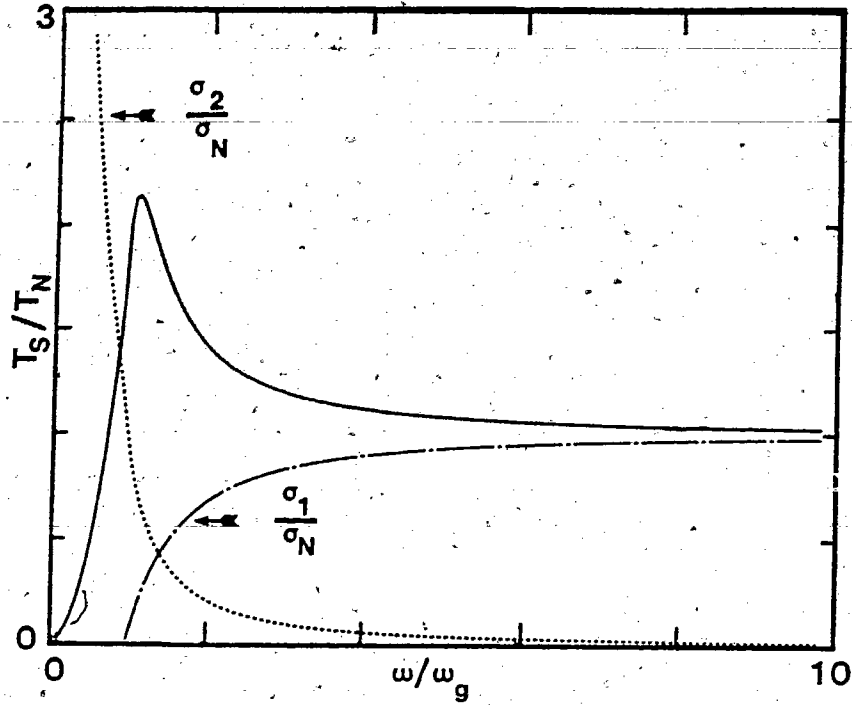


Figure 8

agreement with the observed ratios of Palmer and Tinkham.⁵

The second distinct feature of the theoretical T_S/T_N ratio is the gradual tailing off of the ratio to unity at energies well above the gap energy. At energies well above the gap energy, the influence of the gap will no longer be observable and the superconducting state will behave like the normal state. This feature is in good quantitative agreement with the observed ratios of Palmer and Tinkham.

The experimentally observed ratios presented in Figures 9, 10, and 11 differed from the theoretically calculated ratios in two ways. The first is that none of the experimental ratios approached zero at zero energy. For all of the measurements, $T_S/T_N > 1$ for frequencies down to the observable limit (approximately 5 cm^{-1}) and for frequencies up to a characteristic frequency, from which point onwards, T_S/T_N was approximately equal to unity within the noise limits. This characteristic frequency was not the same for each sample but generally fell in the range of $25\text{-}28 \text{ cm}^{-1}$.

Figure 9

Top: Sample Pb1. Solid line is the observed T_S/T_N ratio; chaindotted line is the modelled T_S/T_N ratio.

Bottom: Same for sample Pb2

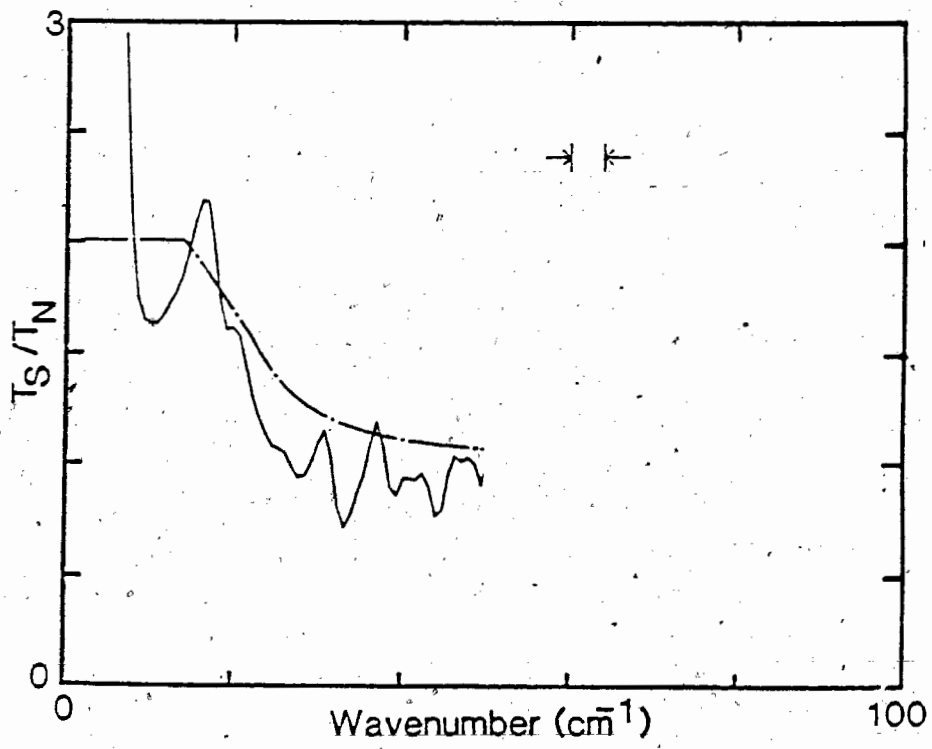
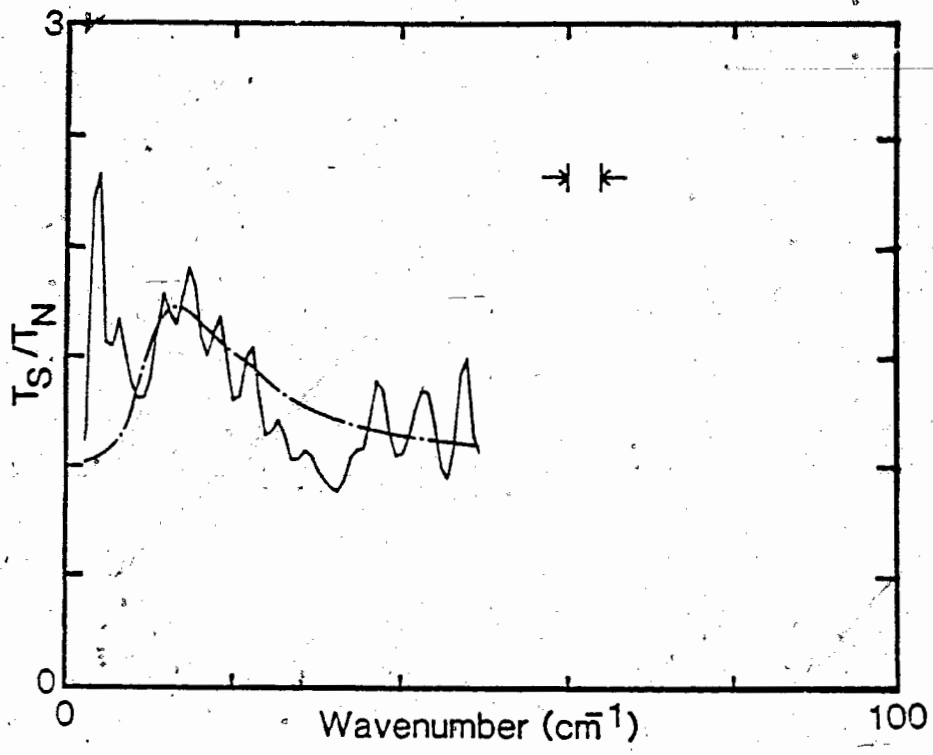


Figure 9

Figure 10

Top: Sample Pb3.

Bottom: Sample Pb4.



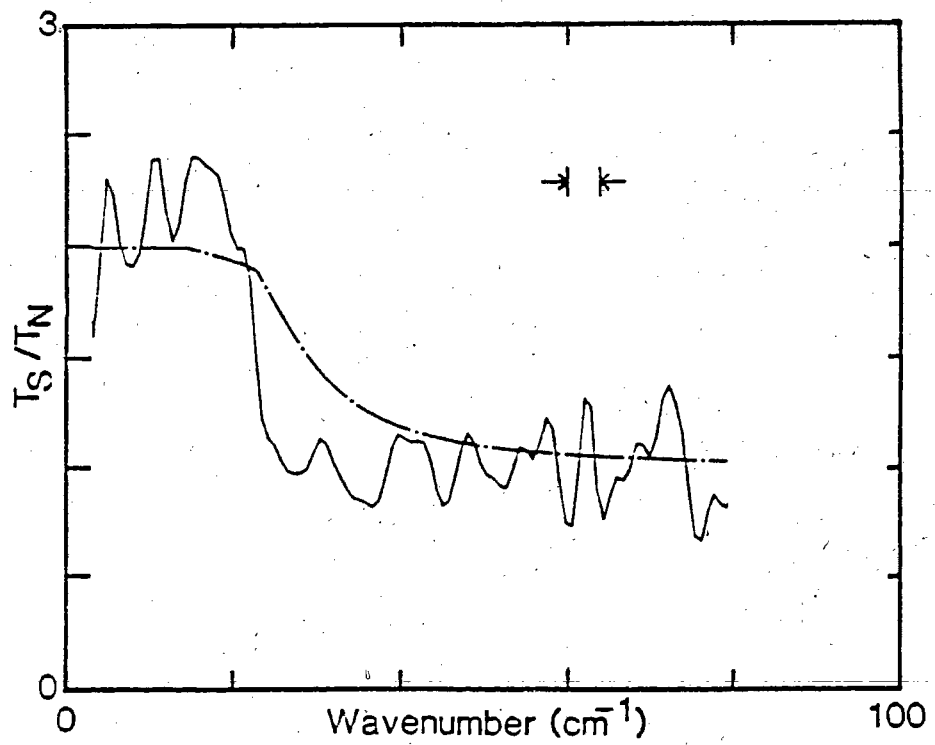
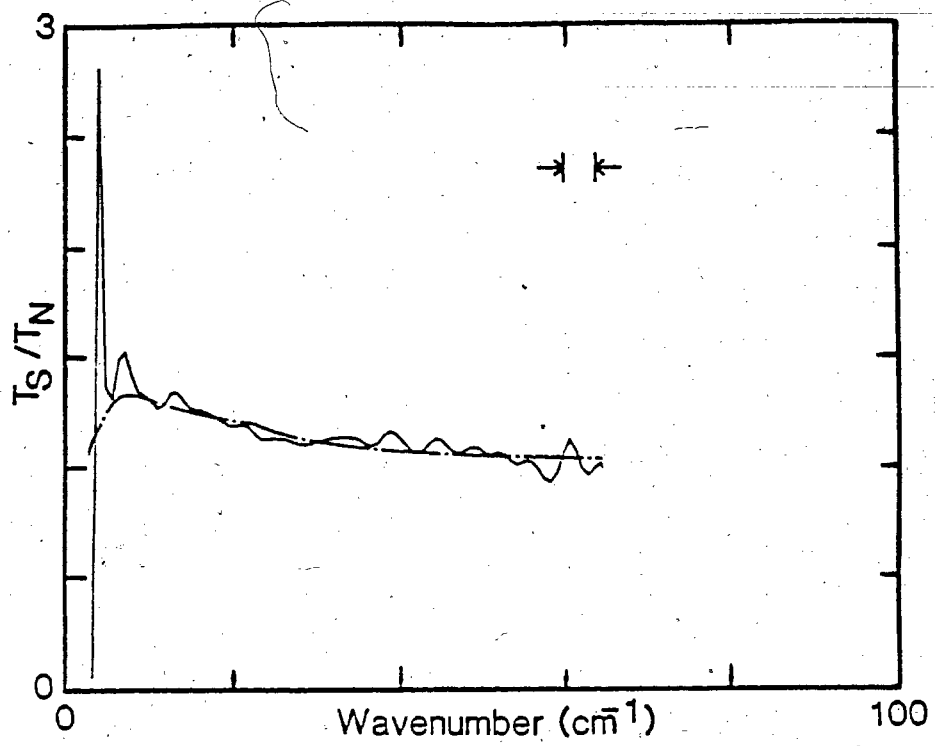


Figure 10

Figure 11

Top: Sample Pb5

Bottom: Sample Pb6

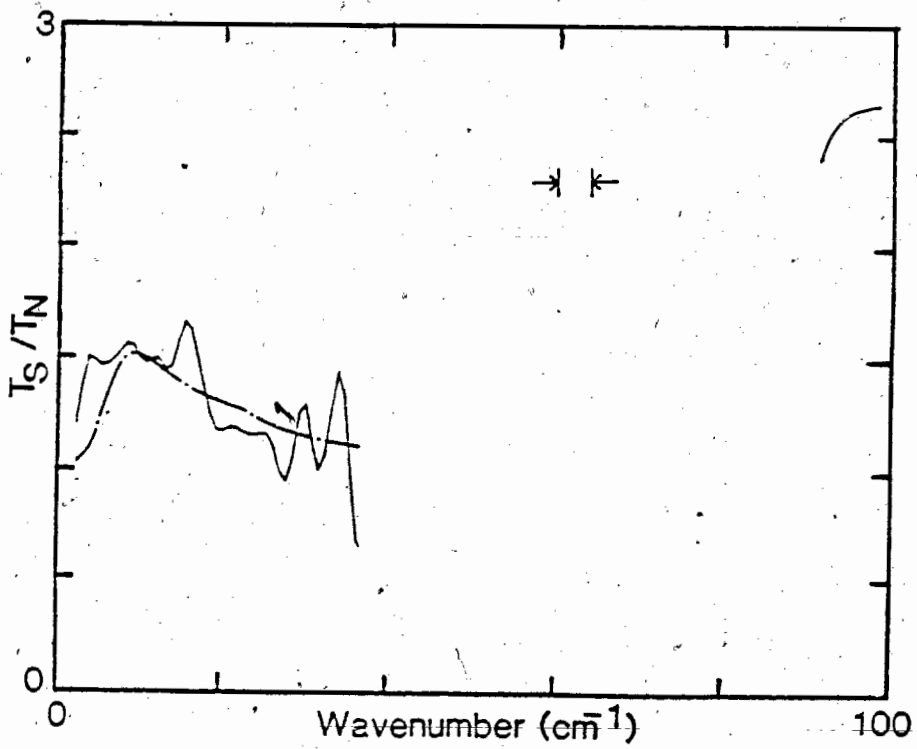
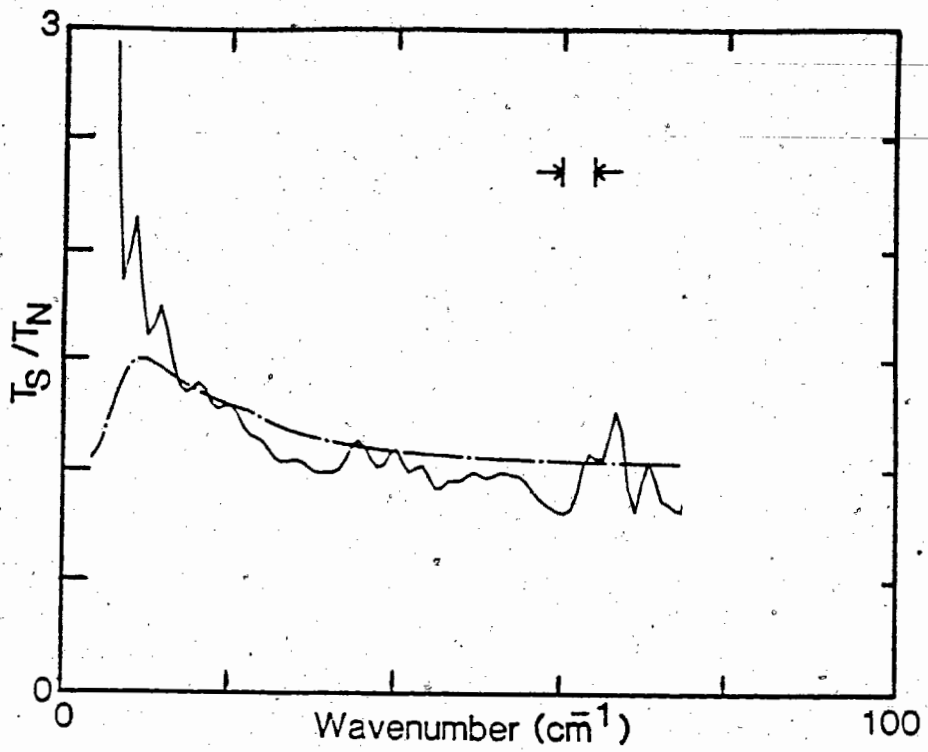


Figure 11

The second difference between the observed T_S/T_N ratios and those predicted by Mattis and Bardeen⁸ was that some of the ratios dropped more rapidly to unity above the previously described characteristic frequency than the calculated ratio. This was especially true for samples designated Pb2 and Pb4.

Analysis of these two characteristics and their implications in view of the Mattis and Bardeen theory have led to the hypotheses that:

- 1) The observed transmission spectra resulted from a superposition of transmission through the grains of the film and transmission through gaps between the grains. The gaps between the grains acted as wave guides for the far-infrared radiation.
- 2) The films were composite in structure with different grains being characterized by different gap values.

The remainder of this chapter will justify the use of these hypotheses and present the mathematical formalism that was used to incorporate these hypotheses into the theoretical models used to fit the experimental T_S/T_N ratios. The quality of the curve-fitting will also be examined.

B. Wave Guide Theory

The formation of the wave guides between the grains could be due to the different coefficients of contraction

of the film and the substrate. Newhouse³² states that films of soft superconductors partially anneal at room temperature, which tends to relieve stresses. On cooling, the film usually contracts more than the substrate. This can cause a tensile stress in the film sufficient to cause plastic deformation. Hence it was hypothesised that the plastic deformation was sufficient to produce openings in the film which acted as wave guides. Although the dimensions of the wave guides were small, with representative dimensions taken from the SEM photographs, with respect to the wavelengths of interest, the incident waves were not totally attenuated. This is due to the thinness of the sample. This assumption shall be shown to be reasonable in the following section.

Using the expression from Lorrain and Corson³³ for an electric field inside a hollow rectangular wave guide with perfectly conducting walls

$$E_x = E_{00x} \sin\left(\frac{n\pi}{b} y\right) \exp i\left(\omega t - \frac{2\pi z}{\lambda_g}\right) \quad (4-1)$$

the attenuation for the wave guide can be calculated if the dimensions of the wave guide and the wavelength of the incident plane are known. b is the width of the wave guide in the y direction. For perfectly conducting walls,

the free-space wavelength for an incident plane wave λ_0 is related to the wavelength of the guided wave λ_{g1} by the following equation

$$\frac{\lambda_{g1}}{\lambda_0} = \frac{1}{\sqrt{1 - \left(\frac{n\lambda_0}{2b}\right)^2}} \quad (4-2)$$

where the different values for n correspond to different modes of propagation and λ_0 is the wavelength of the incident plane wave.

From Eqn. 4-2 we see that the wavelength of the guided wave will be real if the wavelength of the incident plane wave is less than twice the width of the wave guide. This corresponds to unattenuated transmission. If the wavelength of the guided wave is imaginary, the field is attenuated exponentially along the length of the wave guide. If reasonable dimensions for the "wave guide" are taken from the scanning electron microscope photographs and the thickness of the film and the incident wavelength are known, the attenuation of the electric field can be calculated.

The transmitted power is attenuated by the square of the attenuation factor for the electric field. Table 3 gives values for the dimensions of the "wave guides", taken from Table 2, attenuation constants ($k_{g1} = 2\pi/\lambda_{g1}$) and the square of the attenuation factors for $n=1$ and perfectly

conducting walls.

When the film is in the normal state and the finite conductivity of the walls is taken into account, there is additional attenuation due to Joule losses in the walls of the wave guides. Again, the attenuation constant $k_{g2} = 2\pi/\lambda_{g2}$, may be calculated for this case. The attenuation constant for walls of finite conduction is expressed as³³

$$k_{g2} = \frac{1}{a\sqrt{120\sigma\lambda_0}} \left(\frac{1 + \frac{2a}{b} \left(\frac{\lambda_0}{2b}\right)^2}{\sqrt{1 - \left(\frac{\lambda_0}{2b}\right)^2}} \right) \quad (4-3)$$

where a and b are again the dimensions of the wave guide. From this we can calculate the factor, $\exp(-2k_{g2}z)$ by which the average transmitted power is decreased due to the finite conductivity of the walls. Thus the total attenuation constant, $k_T = k_{g1} + k_{g2}$, should be used to calculate the attenuation of the average transmitted power due to the wave guide when the film is in the normal state. Table 4 summarizes the attenuation constants and attenuation factors for both the infinitely conducting case and the finite case for the two samples, Pb3 and Pb4.

Table 3

Attenuation Constants for Perfectly Conducting Walls

Sample	Pb3	Pb4
z (10^{-6} mm)	43.5	49.0
a (10^{-3} mm)	0.12	0.23
b (10^{-3} mm)	1.56	1.11
λ_0 (mm)	1.00	1.00
k_{g1} (mm^{-1})	2000	2800
$\exp(-2k_{g1}z)$	0.84	0.76

Table 4

Attenuation Constants for Finite Conducting Walls

Sample	Pb3	Pb4
k_{g2} (mm^{-1})	500	1100
$\exp(-2k_{g2}z)$	0.80	0.68

Thus for perfectly conducting walls, the average transmitted power through the "wave guide" is 84% of the incident power for sample Pb3 and 76% for sample Pb4. For walls of finite conductivity, 80% of the incident power is transmitted for sample Pb3 and 68% for sample Pb4.

Therefore our hypothesis that the spaces between the grains could act as wave guides is plausible for the dimensions characteristic for our samples.

C. Composite Material

The idea of composite material in dirty superconductors was supported by microwave experiments on granular aluminum films. K. A. Muller *et al.*³⁴ measured DC resistance, microwave loss and cavity frequency shift as a function of temperature. They observed that although the aluminum film had zero DC resistance, the microwave loss decreased below T_C , but did not go to zero. The microwave loss, as the cavity entered the superconducting state, is proportional to the real part of the complex conductivity. They attributed the large excess microwave loss to losses in oxide barriers between grains in the normal and superconducting state. Even though a continuous DC superconducting path existed, the AC fields would still be sensitive to any normal regions.

The application of this idea to the present experiments is as follows. If the real part of the complex conductivity is non-zero below the gap energy, as was measured by Palmer and Tinkham⁵, far-infrared radiation would continue to be absorbed in the film even though there would be a continuous superconducting DC path. Because our films had a critical temperature in agreement³⁶ with the bulk value, a fraction of the grains must have had a critical temperature (and energy gap) like that measured by Palmer and Tinkham ($T_C=7.1K$ and $2 = 22.5 \text{ cm}^{-1}$).


But since the film continued to transmit and not reflect radiation while in the superconducting state at energies well below 22.5 cm^{-1} , there must be a distribution of energy gaps throughout the film. The influence of the other gaps would not be experienced in a DC resistance measurement if there was a sufficient fraction of grains with the 22.5 cm^{-1} energy gap which formed a continuous superconducting path.

D. Modelling of the FIR Data

For the sake of simplicity, each film was modelled as being composed of small (compared to the wavelength of incident radiation) grains that either had the high gap value (22.5 cm^{-1}) or a lower gap value, which was determined by fitting the ratio spectrum. The model film was separated into regions which allowed either transmission through the grains of the film or transmission through spaces between the grains which acted as wave guides. Figure 12 represents this diagrammatically.

Figure 12

Diagrammatic representation of the composite structure of the film showing the grains with different values for the gap and showing the spaces between the grains which act as wave guides. Shaded grains are small compared to the wavelengths of interest.



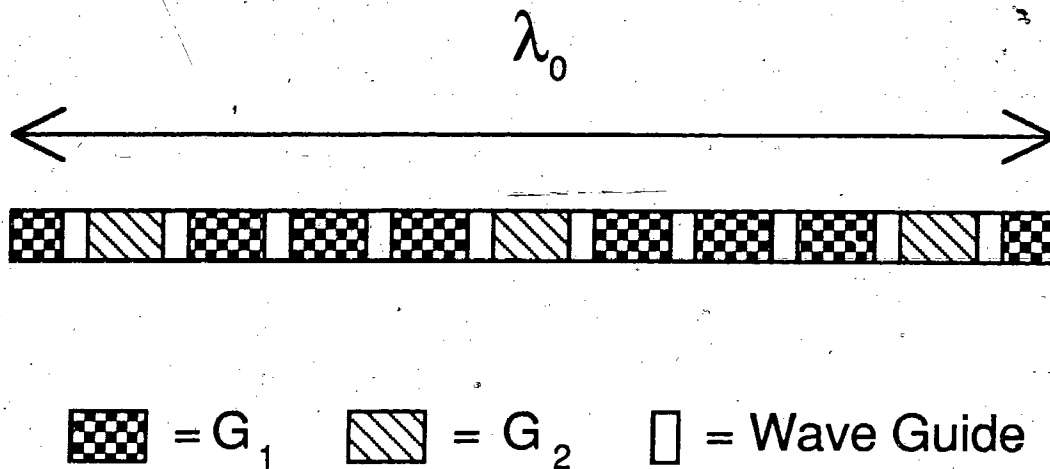


Figure 12

E. Models used to describe the transmission through the grains.

As stated in chapter 1, Mattis and Bardeen⁸ have derived expressions for the complex conductivity for superconducting and normal metals in the extreme anomalous limit. They describe the extreme anomalous limit as the case when the penetration of the field is small compared to the coherence length. For temperatures greater than zero, the expressions must be numerically integrated to obtain values for the complex conductivity. At T=0 K however, the integrals can be evaluated in the form of elliptic integrals. They have the form

$$\frac{\sigma_1}{\sigma_N} = \left(1 + \frac{2\Delta}{h\omega}\right) E(k) - 2 \left(\frac{2\Delta}{h\omega}\right) K(k) \quad (h\omega > 2\Delta) \quad (4-4)$$

$$\frac{\sigma_2}{\sigma_N} = \frac{1}{2} \left\{ \left(\frac{2\Delta}{h\omega} + 1\right) E(k') + \left(\frac{2\Delta}{h\omega} - 1\right) K(k') \right\} \quad (\text{for all } \omega) \quad (4-5)$$

where the arguments of the elliptic integrals E and K are

$$k = \frac{|2\Delta - h\omega|}{|2\Delta + h\omega|} ; \quad k' = (1 - k^2)^{\frac{1}{2}}$$

These calculations have been carried out and the results were shown in Figure 8.

The T_S/T_N ratio can be calculated using the values for the real and imaginary parts of the complex conductivity obtained from the above integrations. This ratio, due to Glover and Tinkham², has the form

$$\frac{T_S}{T_N} = \frac{1}{\left[T_N^{\frac{1}{2}} + (1 - T_N^{\frac{1}{2}}) \left(\frac{\sigma_1}{\sigma_N} \right) \right]^2 + \left[(1 - T_N^{\frac{1}{2}}) \left(\frac{\sigma_2}{\sigma_N} \right) \right]^2} \quad (4-6)$$

This ratio was also plotted in Figure 8.

The ratio of the transmitted power through a thin metal film to that with no film, from Glover and Tinkham, has the form

$$T = \frac{1}{\left| 1 + \sigma d \frac{Z_0}{n+1} \right|^2} \quad (4-7)$$

where d is the film thickness, n is the index of refraction of the substrate and Z_0 is the impedance of free space. Glover and Tinkham state that the effective conductivity of a thin metal film in the normal state is limited by surface scattering and is independent of frequency for the frequencies of interest in the far-infrared. Moreover, they make the approximation that the normal state conductivity has only a real part and is constant. Thus the product of the thickness and the DC conductivity is the reciprocal of the sheet resistance. By measuring the either the DC sheet resistance of the film in the normal

state or by directly measuring the power transmitted through the film by the use of a reference substrate, the T_S/T_N ratio can be calculated provided that the gap frequency is known. Palmer and Tinkham⁵ determined the gap frequency by measuring both the transmission and reflection of the film and from these values they determined the real part of the complex conductivity as a function of frequency. They took as the gap frequency that frequency where the real part of the complex conductivity went to zero.

F. Models used to describe the line shape of the transmission through a "wave guide."

As stated in chapter 1, Richards and Tinkham⁴ and Leslie and Ginsberg¹¹ measured the energy gap of bulk metals. They modelled their absorption edges above the energy gap by the difference between the normal state surface resistance, R_N , and the superconducting state surface resistance, R_S , for the non-resonant cavity. The surface resistance is the real part of the complex impedance and the R_S/R_N ratio can be obtained from the ratio of the superconducting complex impedance to the normal complex impedance, Z_S/Z_N . In the extreme anomalous limit⁸, Z_S/Z_N has the form

$$\frac{Z_S}{Z_N} = \left(\frac{\sigma_N}{(\sigma_1 + i\sigma_2)} \right)^{\frac{1}{3}} \quad (4-8)$$

The complex impedance is related to the surface resistance and the surface reactance by the following equation

$$Z_N = R_N + i X_N = R_N + i\sqrt{3} R_N \quad (4-9)$$

where the square root of three term is specifically for the extreme anomalous limit. R_S/R_N can be extracted from Z_S/Z_N by the following equation⁹

$$\frac{R_S}{R_N} = \operatorname{Re}\left(\frac{Z_S}{Z_N}\right) - \left(\frac{X_N}{R_N}\right) \operatorname{Im}\left(\frac{Z_S}{Z_N}\right) \quad (4-10)$$

After some elementary complex analysis, one obtains

$$\frac{R_S}{R_N} = B \left(\cos\left(\frac{\tan^{-1}(y)}{3}\right) - \sqrt{3} \sin\left(\frac{\tan^{-1}(y)}{3}\right) \right) \quad (4-11)$$

where B and y are given by

$$B = \left[\left(\frac{\sigma_N \sigma_1}{\sigma_1^2 + \sigma_2^2} \right)^2 + \left(\frac{\sigma_N \sigma_2}{\sigma_1^2 + \sigma_2^2} \right)^2 \right]^{\frac{1}{6}}$$

$$y = \frac{\sigma_2}{\sigma_1}$$

R_S/R_N is plotted in Figure 8 using the real and imaginary parts of the complex conductivity calculated from the previous section.

Richards and Tinkham⁴ and Leslie and Ginsberg¹¹ subtracted 1 from the ratio of the power reaching the detector when the cavity was superconducting to the power when the cavity was normal. They then modelled their cavity response above the energy gap by

$$(R_N - R_S)/R_N = -(R_S/R_N - 1) = 1 - R_S/R_N$$

This functional form is unity at the energy gap and falls to zero at energies well above the energy gap.

Since the model presented here demands that T_S/T_N be unity at values well above the energy gap, the response for transmission through a wave guide above the energy gap has the form

$$T_S/T_N = -(R_S/R_N - 2) \quad (4-12)$$

Since it is assumed that R_S is negligible below the energy gap, the T_S/T_N for the wave guide is two up to the energy gap and unity at energies well above the energy gap.

G. Fitting the data

The calculation for the complex conductivity for the composite material is as follows. The real part and the imaginary part will be calculated twice; once for each

value of the energy gap. The real parts are then added together as are the imaginary parts as shown below

$$\sigma_1' = f \sigma_1 (G_1) + (1-f) \sigma_1 (G_2) \quad (4-13)$$

$$\sigma_2' = f \sigma_2 (G_1) + (1-f) \sigma_2 (G_2) \quad (4-14)$$

where $0 \leq f \leq 1$ is the fraction of grains with gap value G_1 . The resultant complex conductivity is then used to calculate the transmission through the grains, according to equation (4-6) and the transmission through the "wave guides", according to equation (4-12). The transmissions are then added together according to the equation

$$T_{\text{Total}} = q T_{\text{grain}} + (1-q) T_{\text{wave guide}} \quad (4-15)$$

where q is the fraction of the transmitted energy through the grains.

H. Fitting procedure and observations

The first step was to choose the lower gap value, G_1 . The upper gap value, G_2 was fixed at 22.5 cm^{-1} . The second step was to choose the fraction of the grains that had this lower gap value. With these two parameters set, the effective complex conductivities could be calculated using Eqns. 4-13 and 4-14. After the complex conductivity was calculated, the transmission ratio due to the transmission through the grains could be calculated using Eqn. 4-6. The resulting transmission ratio was then

plotted onto the observed ratio for comparison. The lower gap value and the fraction of grains with this lower gap value were then adjusted until the best fit was obtained. The criteria for the best fit was my personal judgement as to how well the calculated T_S/T_N ratio followed the observed ratio within the noise level present in each ratio. Then the effect of the transmission through wave guides, calculated using Eqns. 4-12 and 4-15, was added into the model T_S/T_N ratio in order to see if the best fit could be improved. The resulting choice of parameters may not be unique but they represent my best choice given the low signal-to-noise ratio of the observed T_S/T_N ratios.

It was found that the addition of transmission through the "wave guides" caused the model T_S/T_N to drop to unity faster than transmission through grains alone. The samples that had a combination of transmission through the grains and through the wave guides, for example Pb1, appeared to deviate only slightly from the model predictions. It is interesting to note that for the samples that were modelled on transmission through the wave guides alone, the deviation of the model calculation from the observed ratio was the greatest.

It was also found that using two very different values for the gap energy when calculating the effective complex conductivity (equations 4-13 and 4-14) tended to suppress any strong ($T_S/T_N > 1.5$) features in the model T_S/T_N ratios.

Figures 8, 9 and 10 showed the results of these calculations for the fitting parameters shown in Table 5. The value for T_N in equation (4-6) was experimentally determined for all samples except Pb1. For Pb1, T_N was an additional fitting parameter.

Table 5

Fitting Parameters for Transmission Ratio Plots

Sample	f	$G_1(\text{cm}^{-1})$	$G_2(\text{cm}^{-1})$	q	T_N
Pb1	0.9	8.0	22.5	0.5	0.08
Pb2	0.7	14.0	22.5	0.0	---
Pb3	0.9	3.0	22.5	0.5	0.79
Pb4	0.3	14.0	22.5	0.0	---
Pb5	0.9	5.0	22.5	0.5	0.17
Pb6	0.9	5.0	22.5	0.5	0.13

I. Evaluation of model and discussion of results

With the exception of sample Pb3, the model curves did not exactly match the observed excitations within the noise levels present. However, there was a general trend that the excitations followed. Above the energy gap, the T_S/T_N ratios fell to unity more rapidly than the model predicts for all values of parameters. This was especially true for samples Pb2 and Pb4 and to a lesser extent, Pb1 and Pb5. Similar behavior was observed in thin films by Ginsberg and Tinkham.³ Richards and Tinkham⁴ and Leslie and Ginsberg¹¹ also observed a sharp absorption edge above the energy gap for their bulk samples.

The characteristic of suppression of strong features, due to very different values of the gap energies in the calculation of the effective conductivity, was in agreement with the observed T_S/T_N ratio of samples Pb3, Pb5 and Pb6. Thus strong features in the observed ratios would be due to either

- a) transmission through grains that had a single value for the energy gap or grains that were composite in nature but with similar gap energies. This was observed in sample Pb1.
- b) transmission that was dominated by transmission through wave guides. This was observed in samples Pb2 and Pb4.

Thus although we were not able to fit the data by our model within the noise limits present in the data, there were qualitative features of our data which were in agreement with the model.

J. Relation of the model parameters to sample characterization

The origin of a distribution of energy gaps, where G_1 represents a possible lower limit, could be due to the oxidation of the film. The grains of the film could have chemisorbed oxygen when the film was transported to the cryostat from the evaporator. Another possible scheme is that the outer layer of the film is oxidized while the film closer to the substrate is purer. The dirty lead on the surface of the grains or on the outer layer could have a lower gap energy than the pure lead in the interior of the grains or in the layer closest to the substrate.

Carr¹⁰ et. al. have observed broadened DC resistivity superconducting transitions for lead films on sapphire. They also observed voltage steps and reduced critical currents in the I-V properties below T_c . They infer that these steps are characteristic of Josephson devices, providing evidence that the superconducting coupling between grains was weak. We do not observe a broadened DC transition in our samples. Thus the effect of the oxidation on the film on DC transport measurements may

not be detected by our experimental methods; even though the effect of the oxidation may be observable using far-infrared spectroscopy.

From fitting the data, it was found that the sample which had the smallest thickness, Pb3, also had the lowest value for G_1 . It was also found that the thicker samples, Pb1, Pb2, and Pb4, had the higher values for G_1 . This is consistent with the above discussion. Sample Pb6 could also be grouped with samples Pb1, Pb2, and Pb4 with respect to its thickness but it had a low value for G_1 . Either the thickness as measured by the thickness monitor did not accurately represent the thickness of the sample or during the handling of the sample from the evaporator to the cryostat it was exposed to a higher degree of contamination.

One result from fitting the data using the model of a composite film was the indirect determination of the amount of lead with the high gap value that appeared to be present. From the analysis it appeared that there needed to be only approximately 10% pure lead present in the film for a bulk value of the transition temperature. This is

consistent with the observations of Meissner *et. al.*³⁵ on the superconducting transition temperature of lead-bismuth alloys. They found that an alloy composed of 90% (atomic) bismuth still gave a transition temperature above that of bulk lead whereas a concentration of 93% gave a transition temperature lower than the bulk value.

In Table 6 the value for the ratio of the energy gap to the product of the Boltzmann constant and the critical temperature are listed for each sample. Only the higher value of the energy gap (22.5 cm^{-1}) is used.

Table 6

Ratio of Gap Energy to Critical Temperature Values

Sample	T_C (K)	$G_2/k_B T_C$
Pb1	7.11	4.55
Pb2	7.18	4.51
Pb3	7.18	4.51
Pb4	7.33	4.42
Pb5	7.15	4.53
Pb6	7.33	4.42

Chapter 5: Conclusion

A. Summary

The model presented for dirty lead thin films consisted of a film composed of grains with two different energy gaps that allowed transmission through the grains and through the openings between grains. The model used the complex conductivity calculated in the extreme anomalous limit for superconducting and normal metals in order to fit the observed T_S/T_N ratios. The conventional models based completely on transmission through the grains were incapable of fitting the data. The model, while falling short of good quantitative agreement with the observed T_S/T_N ratios, gave qualitative features which agreed with the observed T_S/T_N ratios. This suggests that the overall approach has merit. The measured critical temperature values were in agreement with the literature value within uncertainties for all of the lead films except for sample Pb4.

B. Future experiments

One set of measurements that was not performed was the temperature dependence of the superconducting energy gap. This is important because the BCS prediction is well known. However, an absorption edge like that observed in sample Pb4 is necessary in order to clearly observe the effect in films of the type under study here.

Because the study of lead films occupied the experimental efforts, the far-infrared determination of the superconducting energy gap of lead-bismuth alloy films still needs to be performed. Ideally the transmission and reflection should both be measured in order to experimentally determine the real part of the complex conductivity.

With the introduction of better interferometers, reflectivity measurements on bulk samples may be preferred to transmission measurements on thin films. The advantages in ease of sample preparation should outweigh the difficulty in observing the small change in reflectivity between the normal and superconducting states.

Appendix A

Calculation of Uncertainties

1) Measurement of the critical temperature by DC resistance

The uncertainty in T_C is the reading uncertainty from reading the data plotted on the graph paper. The reading uncertainty was \pm the smallest division on the graph paper, 1mm. This corresponded to different values of uncertainty in T_C due to the different scales used to plot the data.

2) Measurement of the residual resistance

The uncertainty in $R(10\text{ K})$ was $1/2$ the highest minus the lowest values for the resistance taken from the same plots used to determine the critical temperature. The uncertainty in $R(300\text{ K})$ was the reading uncertainty from reading the value from the graph paper. The reading uncertainty was 1mm. The fractional uncertainty in $R(300\text{ K})/R(10\text{ K})$ is the sum of the fractional uncertainties for $R(300\text{ K})$ and $R(10\text{ K})$.

3) Measurement of the transition temperature by the change in magnetization

Four cooling and warming cycles were performed for this sample. During these cycles, the exchange gas was pumped out of the sample chamber and the samples were in better isolation from the main He^4 bath.

There was a lag in the thermal response of the film with respect to the thermal resistor due to the presence of the exchange gas. The change in the thermal response from the first cycle to the last cycle was 0.08 K. This was taken to be the uncertainty in T_C .

4) Measurement of the dimensions of the "wave guides"

Since these were to be representative values, no uncertainty values were given.

List of References

- 1) J. Bardeen, L. N. Cooper, and J. R. Schrieffer, Phys. Rev. 108, 1175 (1957).
- 2) R. E. Glover III, and M. Tinkham, Phys. Rev. 108, 243 (1958).
- 3) D. M. Ginsberg, and M. Tinkham, Phys. Rev. 118, 990 (1960).
- 4) P. L. Richards, and M. Tinkham, Phys. Rev. 119, 575 (1960).
- 5) L. H. Palmer, and M. Tinkham, Phys. Rev. 165, 588 (1968).
- 6) G. L. Carr, S. Perkowitz, and D. B. Tanner, In "Infrared and Millimeter Waves", 13, Academic Press, New York. (1985).
- 7) R. de L. Kronig, J. Opt. Soc. Am. 12, 547 (1926); H. A. Kramers, Atti. Congr. intrn. fis. Como 2, 545 (1927).
- 8) D. C. Mattis and J. Bardeen, Phys. Rev. 111, 412 (1958).
- 9) S. B. Nam, Phys. Rev. 156, 487 (1967).
- 10) G. L. Carr, J. C. Garland, and D. B. Tanner, Phys. Rev. Lett. 50, 1607 (1983).
- 11) J. D. Leslie, and D. M. Ginsberg, Phys. Rev 133, A362 (1964).
- 12) L. Leplae, Phys. Rev. B 27, 1911 (1983).
- 13) D. Karecki, R. E. Pena, and S. Perkowitz, Phys. Rev. B 25, 1565 (1982).

- 14) R. C. Dynes and J. M. Rowell, Phys. Rev. B 11, 1884 (1975).
- 15) J. L. Vossen, and W. Kern, "Thin Film Processes", pg 416. Academic Press, New York. (1978).
- 16) From "How To' Suggestions for Thin Film Deposition", Sloan Instruments Corporation.
- 17) NRC Model-836.
- 18) Sloan Model-DTM 200.
- 19) Lake Shore Cryotronics Model CGR-1-1000-3341C.
- 20) Quantum Technology Model Quantum Cooler 4.2.
- 21) M. W. Denhoff, M. Sc. Thesis, Simon Fraser University, 1981, (unpublished).
- 22) California Fine Wire, 0.003 inch diameter, 12.6 Ohm/ft.
- 23) ISI-DS Model-130.
- 24) Warren Wire Company 0.010 inch diameter #705 S. Nylon formver Manganin, 2.4 Ohm/ft.
- 25) Lake Shore Cryotronics Model-TD500K Silicon Diode.
- 26) B. P. Clayman, Ph. D. Thesis, Cornell University Materials Science Center Report #1026, 1969, (unpublished).
- 27) T. L. Templeton, Ph. D. Thesis, Simon Fraser University, 1973, (unpublished).
- 28) Beckman RIIC Model-FS-720, Serial Number 1047.
- 29) Beckman RIIC Model-LR-100, Serial Number LS 014.

- 30) B. P. Clayman, Microcomputer Experimental Control and Data Analysis for Fourier Transform Spectroscopy, Int. J. of IR and mm Waves, 3, 743-751 (1983).
- 31) Principles of interferometry and their application to far-infrared spectroscopy can be found in G. W. Chantry, "Submillimetre Spectroscopy", Academic Press, London; New York. (1971).
- 32) V. L. Newhouse, "Applied Superconductivity", pg. 144. John Wiley & Sons, New York. (1964).
- 33) P. Lorrain and D. Corson, "Electromagnetic Fields and Waves", W. H. Freeman and Company, San Fransico. (1970).
- 34) K. A. Muller, M. Pomerantz, C. M. Knoedler, and D. A. Abraham, Phys. Rev. Lett., 45, 832 (1980).
- 35) W. Meissner, H. Franz, and H. Westerhoff, Annalen der Physik, 13, 967 (1932).
- 36) B. W. Roberts, Properties of Selected Superconducting Materials, NBS Technical Note 983, (1978).
- 37) J. Bardeen, and J. R. Schrieffer, "Recent Developments in Superconductivity", Progress in Low Temperature Physics, Vol III, New York: Interscience. (1961).
- 38) A. H. Wilson, "The Theory of Metals", pg. 249. Cambridge University Press, New York. (1965).